Amazon Floodplain Water Level Changes Measured with Interferometric SIR-C Radar

Douglas E. Alsdorf, Laurence C. Smith, and John M. Melack

***Abstract*—We find that interferometric processing of repeat-pass L-HH-band shuttle imaging radar (SIR-C) data reveals centimeter-scale changes in the elevations of water surfaces within flooded vegetation. Because radar pulses reflect specularly from the water surface, interferometric observations of open water are incoherent. However, within flooded forests and inundated shrubs, the L-band radar pulse penetrates the vegetation canopy and follows a double-bounce travel path that includes the water and vegetation-trunk surfaces. In these environments, the returned radar energy and associated phase coherence are both stronger than the surrounding nonflooded terrain, permitting determination of the interferometric phase. Phase errors related to atmospheric water vapor are usually longer in wavelength and spatially distinct from phase signatures related to stage changes in tributaries and floodplain lakes. The interferometrically measured stage decreases match gauge data, providing further verification. Water level changes across 150 m to 2.75 km-wide water bodies containing inundated vegetation can be reliably measured. Our results suggest that if future interferometric L-HH-band SAR missions are implemented with short temporal baselines, it is possible to measure the hydrologic response of wetlands and inundated floodplains to changes in mainstem water level.**

***Index Terms*—Amazon basin, SAR interferometry, wetlands hydrology.**

I. Introduction

MEASUREMENTS of river and lake stage are among the most fundamental observations that can be made throughout a watershed. These observations directly impact water resource management, flooding predictions, research on floral and faunal habitats, and our understanding of sedimentation and hydrological processes. Like many remote watersheds, the Amazon basin has few permanent gauging stations. Thus, hydrologic models must rely on sparse observations. Although it is impractical to gauge even a small portion of the floodplain, stage measurements are nevertheless imperative for modeling the temporal and spatial dynamics of water exchange. Remotely sensed observations of the water surface provide an alternative to permanent gauging. Satellite radar altimetry promises measurements of stage elevation accurate to within 10 cm. However, because altimetry is a profiling and not an imaging technique, it is applicable mostly to large water bodies (its height accuracy is limited by orbital, range, and atmospheric errors, [1], [2]). Imagery from spaceborne platforms such as synthetic aperture radars (SAR), passive microwave sensors, and Landsat thematic mapper (TM), have been used to map the extent of inundation [3]–[6], yet these methods do not directly measure stage change or elevation.

Measuring centimeter-scale topographic displacements related to tectonic deformation and flowing glaciers with interferometric SAR is well established [7]–[9]. Because the imaging SAR technique uses an antenna that transmits the radar pulse at an off-nadir look-angle, the high dielectric contrast between smooth open water and air causes most of the pulse energy to be reflected away from the antenna (i.e., specular reflections). However, radar pulse interactions with inundated vegetation typically follow a double-bounce path that includes the water surface and trunks of vegetation, which returns most of the energy to the antenna [3], [10]. In our first report [11], we documented that interferometric processing of L-HH-band SAR data from the Space Shuttle Imaging Radar mission (SIR-C, [12]) produced centimeter-scale measurements of stage change in flooded vegetation. Here, we expand on the brevity of that report by providing the following:

1) interferometric SAR data processing in Sections II and III;
2) possible causes of decorrelation in Section II;
3) detailed interferometric phase and coherence observations over a variety of geomorphologic locations within the Amazon basin in Section IV;
4) a rationale that eliminates the inherent 2π ambiguity in the wrapped phase under certain conditions in Section V.

II. Data Processing, Amplitude and Coherence

As part of the SIR-C mission [12], and in an effort to establish the radar response to inundation and vegetation [3], [10], the Shuttle acquired SAR data in a SW–NE swath crossing the Amazon basin on October 9 and 10, 1994 at local times of 1:14 AM and 12:51 AM, respectively (data takes 142.9 and 158.9) (Fig. 1). L- and C-band data were recorded under a nominal look angle of 35° using combinations of horizontally and vertically transmitted and received polarizations (i.e., L-HH, L-HV, C-HH, and C-HV). The combined C- and L-band amplitude images can be used to map vegetation types and habitats [3], [10], [13] (backscatter composite images are shown in Section IV). The returned energy for the double-bounce path of inundated vegetation is greater than that of open water or nonflooded vegetation [3], [13]. For example, L-HH backscatter amplitudes from flooded forests are greater than for nonflooded forests. Tributaries draining uplands are typically marked by a transition from

Manuscript received September 17, 1999; revised March 17, 2000. This work was supported by NASA, Washington, DC.

D. E. Alsdorf is with the Institute for Computational Earth System Science, University of California, Santa Barbara, CA 93106 USA.

L. C. Smith is with the Department of Geography, University of California, Los Angeles, CA 90024 USA.

J. M. Melack is with the Institute for Computational Earth System Science and Donald Bren School of Environmental Science and Management, University of California, Santa Barbara CA 93106 USA.

Publisher Item Identifier S 0196-2892(01)01161-5.

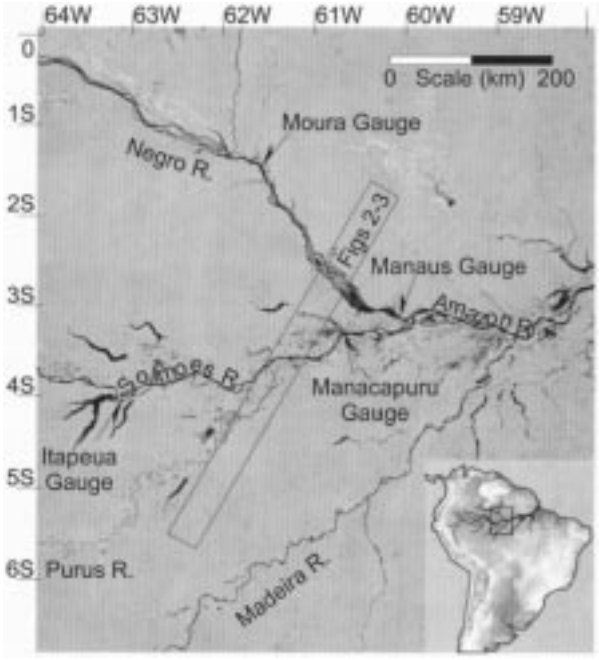

Fig. 1. Mosaic of JERS-1 L-band SAR images over the Amazon [33]. The data were acquired during the low-water period of late 1995. The diagonal box indicates the location of the SIR-C swath.

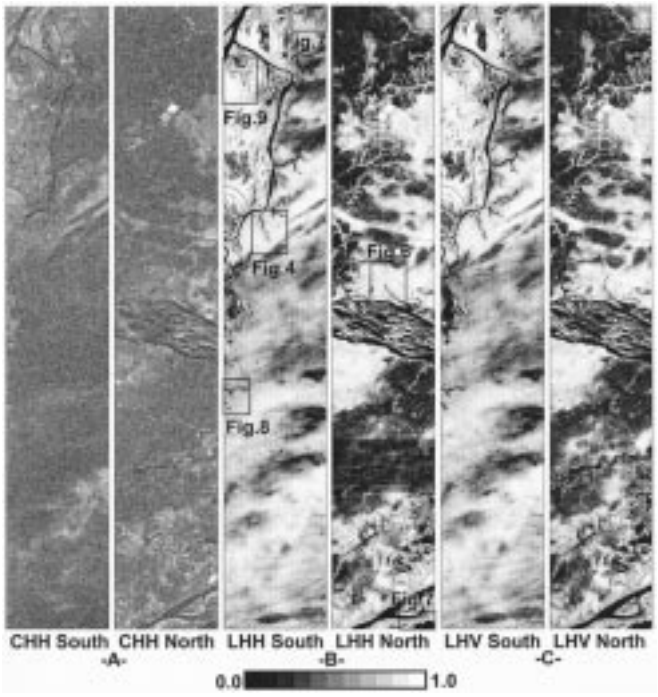

Fig. 2. Coherence images calculated from the (a) C-HH, (b) L-HH, and (c) L-HV SIR-C data. The gray scale index bar and corresponding coherence values are plotted across the bottom. Coherence images are in original radar coordinates and measure 36.3 km × 499.7 km.

forest to flooded forest to open water from upstream to downstream. Emergent shrubs and tree canopies, usually found along the margins of floodplain lakes and channels, cause increased C-HH and L-HH backscattering compared to open water [3], [13].

L- and C-band interferograms were formed by co-registration of the complex radar data to a subpixel accuracy and multiplication of each October 9 complex-valued pixel by the co-registered complex conjugate pixel of October 10 (thus, the interferograms represent the October 9 minus the October 10 phase) [8]. Coherence images were calculated for each interferometric pair using a 3×3 moving window [14], [15] (Fig. 2). The observed coherence is influenced by instrument noise, imaging geometry, and target response effects as well as temporal changes in the scattering elements that comprise the target [14]. For SIR-C, decorrelation resulting from variations in the antenna SNR or from nonparallelism of the two shuttle orbits is minor. There are no obvious long-wavelength changes between the amplitude images that would indicate a daily antenna SNR variation and the angular separation between the orbits is less than 0.03°, which, according to [14], effectively yields no decorrelation. The target itself, such as smooth, open-water surfaces, may yield a low returned energy and thus a localized low SNR that produces low correlation between successive radar images. The remaining source of decorrelation is a function of the temporal changes in the scattering elements that comprise individual pixels. As expected [16]–[19], random spatial changes in the relative positions of the scattering elements during the 24 h between SIR-C acquisitions results in significant decorrelation at C-band (e.g., leaves and small branches of the forest canopy are easily moved by passing winds). At L-band, the scattering elements (e.g., vegetation trunks and earth) are not easily reoriented in one day. Instead, temporal decorrelation likely results from changes in soil moisture. Low coherence in the L-band data is found in some lowland areas and in broader regions where local rainfall may have increased the moisture content of the scattering elements. Table I summarizes the coherence observations for various regions in the SIR-C data. Open-water is marked by poor correlation at both C- and L-bands, while forested regions demonstrate higher coherence at L-band than at C-band. Over flooded vegetation, L-HH coherence is greater than L-HV. Thus, we used the L-HH interferometric data for the phase analysis in Sections III and IV.

TABLE I
COHERENCE VALUES FOR SELECTED REGIONS

Location	avg. LHH	σ LHH	avg. LHV	σ LHV	avg. CHH	σ CHH
Entire Interferogram	0.57	0.21	0.57	0.21	0.29	0.14
Open Water (rivers)	0.27	0.14	0.28	0.14	0.26	0.13
Non-Flooded Uplands	0.61	0.20	0.57	0.20	0.28	0.14
Non-Flooded Lowlands	0.71	0.18	0.66	0.19	0.31	0.15
Flooded Vegetation	0.69	0.21	0.58	0.21	0.30	0.15

Inundated forests and floodplain lakes and channels with emergent shrubs are not only marked by high backscatter amplitudes but also by strong L-band interferometric phase coherence (Table I). Because the L-band radar pulse follows a double-bounce travel path within flooded vegetation, both the vegetation trunks and water surface must maintain their relative scattering positions within a pixel to preserve temporal coherence. Compared to a smooth water surface, wind- or wave-roughened water surfaces result in both stronger radar returns, especially at C-band, and stronger temporal decorrelation [20]. However, the open-water surfaces of the Amazon and Purus Rivers are marked by the lowest returns in the L-band data. Thus, it seems unlikely that roughened conditions would

be found within the flooded vegetation where the canopy and trunks buffer both wave and wind action. Random growth of individual vegetation trunks within a pixel element may cause some decorrelation, yet this effect is presumably quite small during the one-day separating the SIR-C data takes. Taken together, the strong L-band coherence distributed uniformly over flooded vegetation permits reliable interferometric phase measurements of the water and vegetation surfaces.

III. Interferogram Flattening and Phase Unwrapping

Removal of the interferometric phase associated with viewing parallax over a spherical surface, the "flat-earth" phase, from the L-HH-band interferogram requires accurate knowledge of the SIR-C baseline and its changes throughout the image [8]. Based on the orbital position data provided by the SIR-C mission, the perpendicular and parallel baseline components at mid-swath are $+48$ m and $+17$ m, respectively. Using this baseline to flatten the interferogram leaves a residual phase with a trend that does not mimic topography, thus indicating inadequate flattening. Alternatively, the perpendicular component of the baseline can be estimated based on the number of phase cycles within a measured slant range distance [21]. In this case, the mid-swath perpendicular baseline component increases to $+63$ m and more completely removes the flat earth phase compared to the shorter baseline [Fig. 3(a)]. Still, a residual phase persists in the interferogram that cannot be removed by further simple adjustments to the baseline.

After flat-earth phase removal, the interferometric phase measures both topography and any changes in the apparent radar range. Changes in range can be caused by variations in propagation conditions or by pixel position changes in the terrain. The amount of topographic relief captured by one phase cycle, from $-\pi$ to $+\pi$, is a function of the perpendicular component of the baseline [8], [17]. Short perpendicular components yield more topographic relief per phase cycle than long baselines. Based on 1 : 100 000 scale topographic maps of the Amazon basin [22], the total relief within the SIR-C swath is less than $\sim$65 m. For L-band, this range in relief will be fully captured by one phase cycle if the mid-swath perpendicular baseline component is $\sim$250 m or less [8], [17]. The flattening tests demonstrate that the correct SIR-C perpendicular baseline at mid-swath is close to $+63$ m, considerably less than 250 m. Thus, after flattening, the topographic component of interferometric phase should not exceed one cycle across the SIR-C data.

To remove the excess phase cycles from an individual interferogram, we

1) flattened the interferogram with the $+63$ m perpendicular baseline [$+17$ m parallel, the baseline slowly varies in both the along and across orbit directions, i.e., Fig. 3(a)];
2) performed phase unwrapping with an algorithm that avoids propagating local phase errors into global errors [23];
3) fit a low order polynomial surface to the unwrapped interferogram;

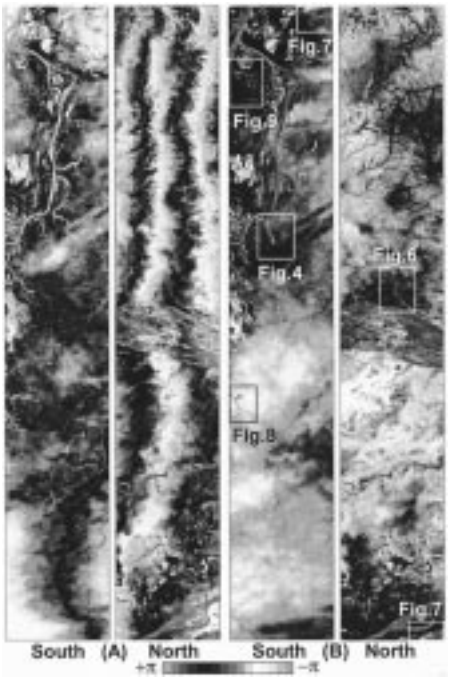

Fig. 3. L-HH flattened interferogram using (a) a $+63$ m perpendicular and $+17$ m parallel mid-swath baseline and (b) L-HH flattened wrapped interferogram using the baseline in (a) and subtracting a first order polynomial surface. The interferogram in (a) is not adequately flattened. Interferometric phase values from (b) are used in Figs. 4 and 6–9. Interferograms are in original radar coordinates and measure 36.3 km $\times$ 499.7 km.

4) calculated the modulo 2π phase of the surface and subtracted it from the wrapped but flattened interferogram of step 1.

Selection of the polynomial order is subjective. The derived surface should only encompass the long-wavelength residual phase (low order polynomials) and not match the short-wavelength topographic phase of stream valleys and floodplain channels (high order polynomials). We chose a first order polynomial that, after flattening and subtracting, produced a wrapped interferogram free of the long-wavelength residual phase [Fig. 3(b)].

Generally, phase unwrapping is necessary when more than one phase cycle is required to image the topographic relief or when the displacement field exceeds half of the SAR wavelength. Because the SIR-C baseline is small and Amazon relief is low, phase unwrapping is unnecessary for constructing a DEM. However, short baselines also yield inaccurate DEMs [24]. Furthermore, the SIR-C interferogram is corrupted by phase distortions related to atmospheric water vapor, which further prevents the construction of an accurate DEM [19], [25], [26]. Therefore, we did not attempt to construct a DEM from the SIR-C data. For displacement comparisons with the wrapped phase (discussed in Sections IV), we unwrapped [23] the polynomially flattened interferogram.

IV. Interferometric Phase Comparisons

The polynomially flattened L-HH interferometric phase measures the topographic relief as well as any changes in the apparent radar range that occurred during the 24 h between the SIR-C acquisitions. Typically, these components are separated by subtracting the topographic phase either modeled from a

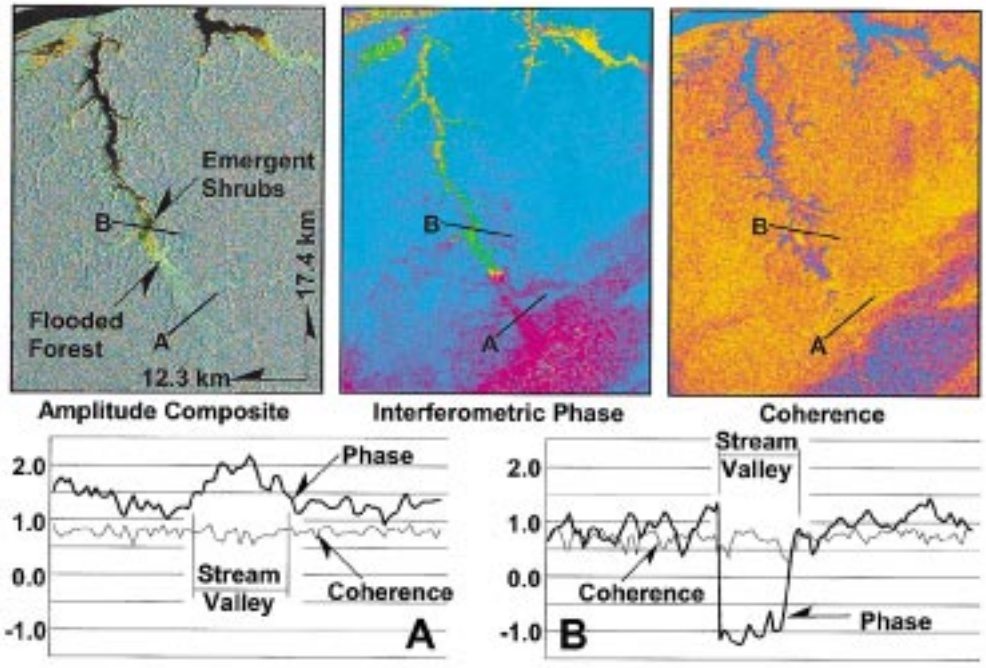

Fig. 4. (Left) Amplitude composite, SIR-C C-band HH-polarization intensities are colored red and L-HH are green, and L-HV are blue, (middle) polynomially-flattened wrapped interferograms [i.e., extracted from Fig. 3(b)], and (right) coherence [i.e., extracted from Fig. 2(b)] images for a tributary of the Purus River. Profiles of phase and coherence values extracted from the images show the (a) the valley topography in and (b) one-day stage decrease across inundated vegetation. Atmospheric distortions run diagonally across the lower-right in the phase and coherence images.

pre-existing DEM ("two-pass" method [9]) or observed in an additional interferogram ("three-pass" method [8]). Unfortunately, the only digital topography data set available for our study area is a low resolution, 1-km posting DEM that fails to image the subtle terrain of Amazon tributary valleys. Other SIR-C baselines are too large for interferometric analysis. Instead, because the perpendicular baseline component is short, we can use simple physiographic comparisons to visually separate the phase components. The short, +63-m mid-swath perpendicular baseline component indicates that 0.5 radians are equivalent to 18.5 m of topographic relief [8], [17]. The orientation of the baseline indicates that phase peaks are indicative of topographic valleys and phase troughs map to topographic ridges. Because the October 10 SAR image was subtracted from the October 9 image, troughs (peaks) in the interferometric phase can also indicate an increase (decrease) in the apparent radar range from the October 9 to October 10. Thus, using (1), where $\lambda = 24.0$ cm, $\varphi =$ the displacement phase, look angle $= 35.2°$, and $\Delta z =$ vertical displacement, 0.5 radians of interferometric phase are also equivalent to 1.2 cm of purely vertical displacement of the topographic surface

$$\Delta z = \frac{\lambda \varphi}{4\pi \cos(lookangle)}. \tag{1}$$

Using the +63-m mid-swath perpendicular baseline component to measure the expected ~65 m of total topographic relief indicates a maximum variation in the topographic interferometric phase component of 1.75 radians. The average coherence values between 0.6 and 0.7 (Table I) yield expected phase noise values of 0.35 to 0.25 radians, respectively, for the ten looks used in the processing [14], [15]. In general, the phase values over the nonflooded areas in Fig. 3(b) are distributed from +0.75 to −1.5 radians, falling within the expected 1.75 range if the related phase noise is included. In the following sections, we use profiles extracted from the L-HH interferogram to compare and separate the topographic and displacement phase components.

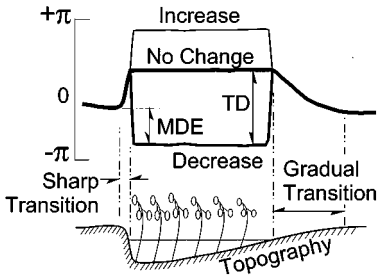

Fig. 5. Schematic cross section of a lake or tributary including the shoreline topography and inundated vegetation with expected interferometric phase values for decreasing, no-change, and increasing water levels. Schematic assumes a small baseline and small stage decrease such that the total phase does not exceed 2π. Phase transitions from surrounding topography to the water surface are noted on the schematic. Minimal decrease estimates (MDE) of the phase are found across sharp transitions, whereas the true decrease (TD) is measured across gradual transitions (see text for details).

A. Interferometric Phase Across Upland Tributaries

The upland tributary in Fig. 4 discharges to the Purus River and incorporates inundated emergent shrubs and flooded forest as well as nonflooded forest in the upper reaches. As expected, the phase values across the nonflooded portion of the tributary are peaked where crossing the topographic valley (profile A), yet, where crossing the flooded vegetation in the same valley further downstream (profile B), the phase values exhibit significant local troughs. Coherence values in both cases are typ-

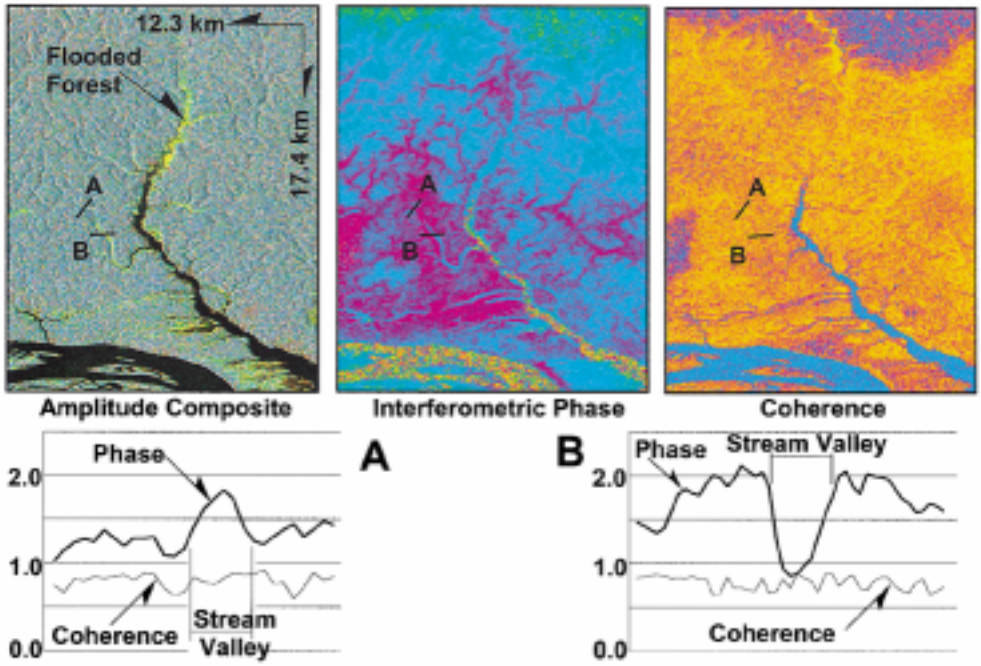

Fig. 6. (Left) Amplitude composite, (middle) polynomially-flattened wrapped interferogram, and (right) coherence images for a tributary of the Negro River. (a) Profiles of phase and coherence values extracted from the images show the valley topography and (b) one-day stage decrease across inundated vegetation. Compared to Fig. 4, this tributary is much smaller yet still yields reliable observations of stage decrease.

ically greater than 0.5. Thus, the phase trough cannot be related to poor coherence. Because the trough amplitude is about twice that of the phase peak, interpreting the trough as a topographic ridge would require significant positive relief within the middle of the valley. The amplitude composite does not show such a ridge. Furthermore, the phase trough in the interferogram image extends across both emergent shrubs and flooded forest. Thus, variations in plant physiology cannot be responsible for the anomalous trough. Atmospheric water vapor can cause kilometer-scale spatial variations with millimeter to decimeter length errors in the interferometric phase [19], [25]. This effect is likely responsible for the long-wavelength offset between the phase profiles (note the ∼0.5 radian overall difference in phase values and the ∼east-trending red colored phase values with poor coherence). Although observations from optical data (TM and airborne videography) have shown small spatial-scale changes in atmospheric water vapor from evaporation over open water or from plant transpiration, advection diffuses the boundaries of these systems well beyond the confines of stream valleys and lake basins. Therefore, the trough is not related to topography nor to error sources. Instead, it likely represents a surface displacement moving away from the shuttle during the two SIR-C acquisitions.

Water levels within the Purus were falling during the October SIR-C acquisitions and the clear connection between the tributary and the Purus presumably allows for local water evacuation. Thus, the phase trough likely represents a drop in the tributary water level within the inundated vegetation. Unfortunately, the lack of a high-resolution DEM or a third SIR-C pass prohibits a straightforward measurement of the stage decrease represented by the phase trough. Instead, we note that the upstream profile in Fig. 4 marks the valley topography with a ∼1.0 radian peak. If this same peak occurred along the downstream profile (i.e., assuming the valley cross section is similar), then we can convincingly expect at least a ∼2.0 radian decrease in tributary stage (Fig. 4). Since the water surface elevation change is purely vertical, the 2.0 radian trough can be projected from the SAR line-of-sight direction using (1) to yield a stage decrease of about 5 cm.

The accuracy of this displacement measurement is a function of the local coherence and of our ability to separate the topographic phase component from the total observed phase. Coherence values in Fig. 4, as well as in the following figures, are almost always greater than 0.5, which is equivalent to a ∼0.5 radian error (given the ten looks used in the processing, [14], [15]) or less than 1.2 cm of vertical displacement. Qualitatively, pixel-to-pixel phase variations in profiles A and B (Fig. 4) are less than 0.5 radians, in agreement with the coherence-estimated error. The shorelines of tributaries and floodplain lakes include both sharp (left side, Fig. 5) and gradual transitions from land to water (right side, Fig. 5). If the water level remains constant between SAR acquisitions, then the total phase consists only of the topographic component, and it will mirror image the topography and unchanging water surface (provided double-bounce returns). If we can measure the topographic phase within the transition zone, e.g., gently sloping regions crossing several pixels (right side, Fig. 5), then the stage decrease estimate approaches the true change. Comparing the phase trough with the topographic phase outside of sharp transition zones yields a minimal estimate of stage decrease. Taken together, these error sources suggest a displacement measurement accuracy that varies with local morphology but can be generally placed at ± 1.0 cm.

The upland tributary in Fig. 4 is 500-m-wide. However, stage decreases in smaller streams can also be reliably measured.

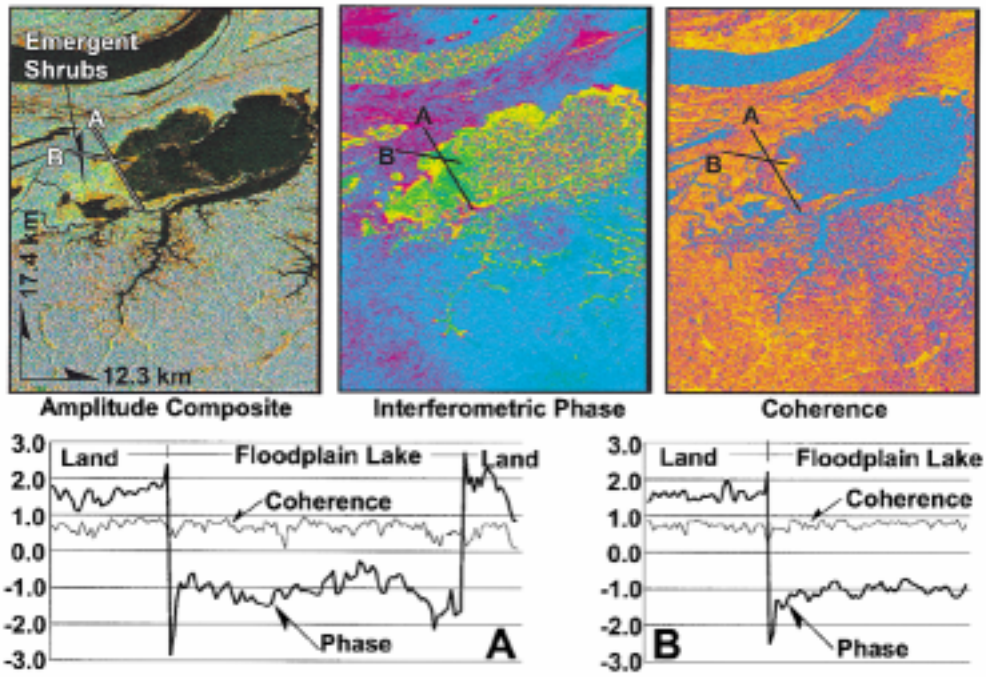

Fig. 7. (Left) Amplitude composite, (middle) polynomially-flattened wrapped interferogram, and (right) coherence images for a large floodplain lake immediately adjacent to the Solimões-Amazon River. Profiles of phase and coherence values extracted from the images show one-day stage decrease across inundated vegetation. The shorelines of this lake are well defined. Thus, the phase shows a sharp transition from land to water (e.g., the left side of Fig. 5).

The upland stream in Fig. 6 measures ∼150 m in width and is marked by a 1.0 radian trough. Like Fig. 4, the coherence across both profiles in Fig. 6 is strong, yielding reliable interferometric phase measurements. Accepting the previous discussion for the Purus tributary yields a 2.0 to 3.0 cm stage decrease in the Negro tributary (Fig. 6).

B. Interferometric Phase Across Floodplain Lakes

The margins of most floodplain lakes include emergent shrubs that provide substantial double-bounce radar returns. For example, high amplitudes and strong coherence mark the western edge of the lake in Fig. 7, where emergent vegetation is known from *in-situ* observations and aerial reconnaissance [13]. Interferometric phase values show a trough approaching 3.0 radians in relief, located only within the flooded vegetation. Phase values over the land surface clearly exceed those over the lake, and the phase transition from land to water is coincident with the expected increase in amplitude returns. Remarkably, the phase trough spans 2.75 km with only a slight undulation. Thus, we estimate the decrease in lake water level during the 24 h separating the SIR-C acquisitions at ∼7.0 cm.

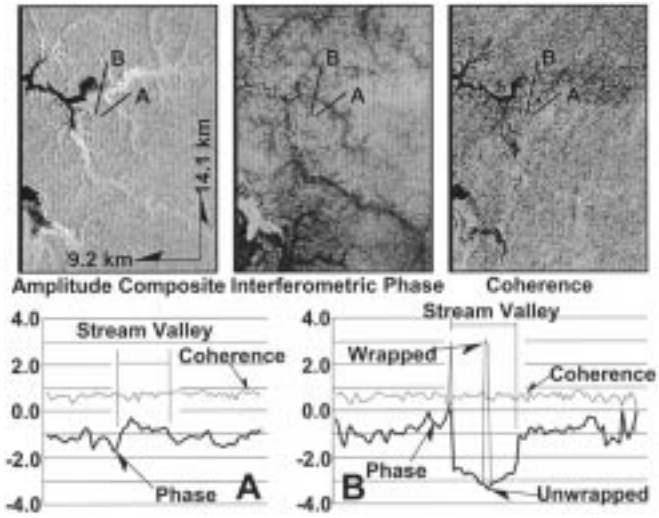

Fig. 8. (Left) Amplitude composite, (middle) polynomially-flattened wrapped interferogram, and (right) coherence images for a tributary of the Purus River. (a) Profiles of phase and coherence values extracted from the images show the valley topography and (b) shows one-day stage decrease across inundated vegetation. Phase unwrapping correctly identifies the $-\pi$ to $+\pi$ to $-\pi$ spike in the center of the trough and extends it to -3.4 radians.

C. Phase Unwrapping

Phase unwrapping may be necessary to clarify stage changes when the average local phase is nonzero. In these cases, a phase trough (peak) wraps from $-\pi$ to $+\pi$ ($+\pi$ to $-\pi$). For example, the mean local phase in the plots of Fig. 8 is about -1.0 radian. Thus, any stage decrease in excess of 2.0 radians will wrap from $-\pi$ to $+\pi$. The spike at the center of the phase trough in plot B (Fig. 8) is associated with strong coherence values (0.5 to 0.7). Thus, it is not related to noise (the spike along the valley edge is marked by poor coherence, 0.0 to 0.3, and is noise related). Unwrapping the phase with a two-dimensional (2-D) algorithm [23] applied to the interferometric image correctly identifies the $-\pi$ to $+\pi$ to $-\pi$ spike and extends the trough to -3.4 radians. The phase relief across the trough is about 2.5 radians, giving a local stage decrease of 5.0 to 6.0 cm.

If water level changes exceed 14.7 cm [using 2π as the displacement phase in (1)], then phase unwrapping will be necessary to resolve the inherent 2π ambiguity. In cases where the

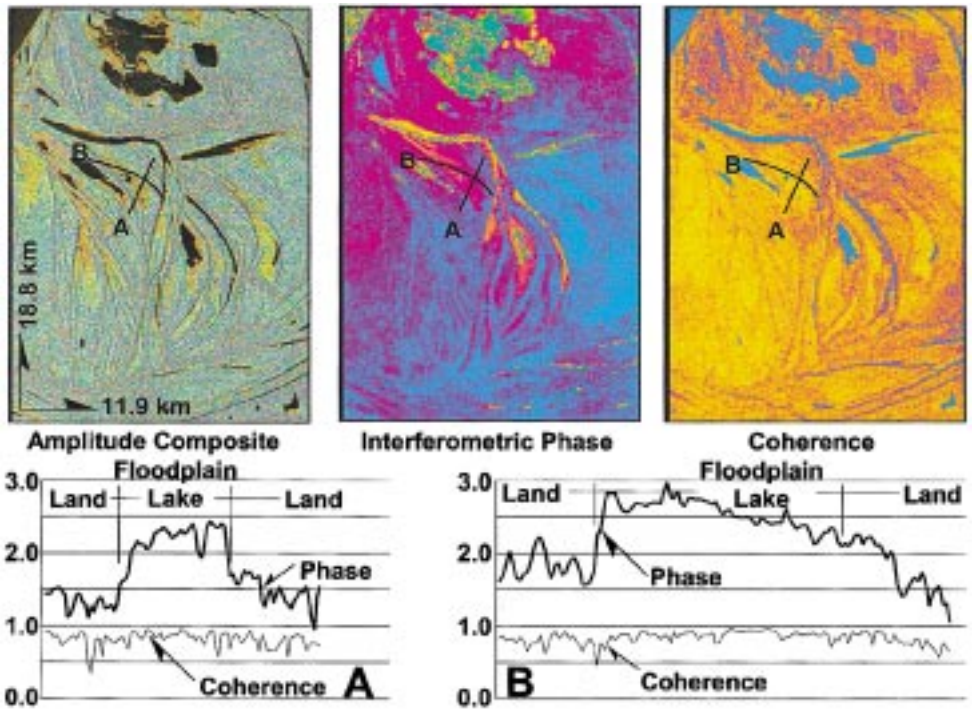

Fig. 9. (Left) Amplitude composite, (middle) polynomially-flattened wrapped interferogram, and (right) coherence images for floodplain lakes near the confluence of the Purus and Solimões-Amazon Rivers. Profiles of phase and coherence values extracted from the images do not show stage decreases, rather, the phase plots are indicative of nonchanging conditions.

transition zone is gradual (right side, Fig. 5), large water-level changes may be distributed across a number of pixels that incorporate each 2π cycle, thus allowing accurate phase unwrapping. In other cases, where the transition is sharp and coherence may be poor, accurate phase unwrapping will be difficult because a number of 2π cycles may occur across just one or two pixels. For example, the transition zones of the stream in Fig. 4 are sharp and marked by poor coherence, so although phase unwrapping produces the same result as the given wrapped phase, the 2π ambiguity remains. Our interpretation of a $\sim$5 cm water level decrease could be incorrect by additional integer multiples of $\pm$14.2 cm. In the example of Fig. 6, the transition zones are similar in width to those of the stream in Fig. 4 (note that the phase plots are different in scale), but the stronger coherence and lesser change in phase suggest that additional 2π phase cycles are unlikely in Fig. 6.

D. Floodplain Lakes With No Stage Decrease

Although most of the tributaries and floodplain lakes show interferometric phase values indicative of stage decrease, some water bodies demonstrate no change in water levels. As evident in the radar amplitude image of Fig. 9, several floodplain lakes near the confluence of the Purus and Solimões-Amazon Rivers are choked with vegetation and have no apparent open-water pathway connecting the lakes with either river. Profiles extracted across one of these lakes show remarkably strong coherence as well as positive phase relief. The scrollbar morphology of this lake suggests a topography including both sharp land-to-water transitions (perpendicular to the lake, i.e., plot A of Fig. 9) and gradual shorelines (parallel to the lake, i.e., plot B of Fig. 9). Both phase plots agree with this topography: plot A is similar to the left side of the schematic in Fig. 5 while plot B is similar to the right side.

V. Results and Conclusions

Using the method described in Section IV, stage changes for vegetation covered floodplain lakes and tributaries in flooded forests were measured throughout the SIR-C interferometric swath. The greatest drops of 7 to 11 cm were found in water bodies closest to the mainstem Purus, Solimões-Amazon, and Negro Rivers. For comparison, the Manaus gauge (Fig. 1) recorded a 12-cm drop in water level from October 9 to October 10, 1994 and an average daily decrease of 12 cm in the previous seven days. Gauges at Manacapuru, Itapeua, and Moura (Fig. 1) recorded decreases of 7 cm, 5 cm, and 6 cm, respectively, while averages over the previous seven days were 11 cm, 7 cm, and 11 cm, respectively. Day-to-day variations along these mainstem rivers, from the peak of the 1994 flood in early July to the SIR-C acquisitions in October, rarely exceed 15 cm.

The inherent 2π phase ambiguity in some of the interferometric measurements can be hydrologically checked against the known mainstem gauge records. For example, the interferometrically measured water level of the stream in Fig. 4 could have increased by 9.2 cm, decreased by 5.0 cm, or decreased by 19.2 cm (additional integer multiples of $\pm$14.2 cm are also possible). In October, the peak of the flood wave has passed the SIR-C swath location, and water levels within the Solimões-Amazon are the dominant control on water levels across the floodplain [6], [27]. Given that water levels on the mainstem are decreasing

at an average rate of 7 to 12 cm per day, it is unlikely that floodplain water levels decreased 19.2 cm or more. Although inundated vegetation can cause water ponding resulting in increased water levels, the proximity and connectivity of the stream to the Purus River suggests that evacuation of the stream is possible, which would yield decreasing water levels. Thus, we interpret the interferometric observations in Fig. 4 to indicate $\sim$5 cm of water level decrease. Similar arguments can be applied to the other interferometric observations.

The centimeter-scale measurements of stage change exactly co-registered with a 25-m-scale SAR image provides new observations of hydrologic exchange between tributaries, floodplains, and mainstem rivers. The sparse Amazon gauge network provides hydrologic measurements along mainstem rivers, yet our interferometric SIR-C observations are located on nearly every tributary and floodplain lake greater than a couple of hundred meters in size. This yields an immense improvement not only in measurement density but also provides observations over tributaries and inundated floodplains.

Because the centimeter-scale accuracy of the interferometric measurement is small enough to gauge the average daily changes in water levels, our understanding of the daily flux between floodplains and rivers should benefit from future interferometric L-HH SAR observations. For example, repeat-pass airborne interferometric SAR missions [28], [29] coupled with sparse ground observations could yield a dense set of reliable measurements used to build models relating runoff and infiltration to water storage and evacuation across an entire watershed. Given that 140 000 km^2 along the Amazon mainstem and four of its major tributaries are annually subjected to flooding [30] and that wetlands cover 5–6 million km^2 globally [31], [32], a vast area could be targeted for large-scale satellite-based interferometric SAR observations.

ACKNOWLEDGMENT

The authors would like to thank L. L. Hess, L. A. K. Mertes, and T. Dunne for their collaboration on this research.

REFERENCES

[1] C. M. Birkett, "The contribution of TOPEX/POSEIDON to the global monitoring of climatically sensitive lakes," *J. Geophys. Res.*, vol. 100, pp. 25 179–25 204, 1995.

[2] C. M. Birkett, "Contribution of the TOPEX NASA radar altimeter to the global monitoring of large rivers and wetlands," *Water Resources Res.*, vol. 34, pp. 1223–1239, 1998.

[3] L. L. Hess, J. M. Melack, S. Filoso, and Y. Wang, "Delineation of inundated area and vegetation along the Amazon floodplain with SIR-C synthetic aperture radar," *IEEE Trans. Geosci. Remote Sensing*, vol. 33, pp. 896–904, July 1995.

[4] L. C. Smith, "Satellite remote sensing of river inundation area, stage, and discharge: A review," *Hydrolog. Processes*, vol. 11, pp. 1427–1439, 1997.

[5] L. A. K. Mertes, D. L. Daniel, J. M. Melack, B. Nelson, L. A. Martinelli, and B. R. Forsberg, "Spatial patterns of hydrology, geomorphology, and vegetation on the floodplain of the Amazon River in Brazil from a remote sensing perspective," *Geomorphology*, vol. 13, pp. 215–232, 1995.

[6] S. J. Sippel, S. K. Hamilton, J. M. Melack, and E. M. M. Novo, "Passive microwave observations of inundation area and the area/stage relation in the Amazon River floodplain," *Int. J. Remote Sens.*, vol. 19, pp. 3055–3074, 1998.

[7] R. M. Goldstein, H. Engelhardt, B. Kamb, and R. M. Frolich, "Satellite radar interferometry for monitoring ice sheet motion: Application to an Antarctic ice stream," *Science*, vol. 262, pp. 1525–1530, 1993.

[8] H. A. Zebker, P. A. Rosen, R. M. Goldstein, A. Gabriel, and C. L. Werner, "On the derivation of coseismic displacement fields using differential radar interferometry: The Landers earthquake," *J. Geophys. Res.*, vol. 99, pp. 19 617–19634, 1994.

[9] D. Massonnet, M. Rossi, C. Carmona, F. Adragna, G. Peltzer, K. Feigl, and T. Rabaute, "The displacement field of the Landers earthquake mapped by radar interferometry," *Nature*, vol. 364, pp. 138–142, 1993.

[10] Y. Wang, L. L. Hess, S. Filoso, and J. M. Melack, "Understanding the radar backscattering from flooded and nonflooded Amazonian forests: Results from canopy backscatter modeling," *Remote Sens. Environ.*, vol. 54, pp. 324–332, 1995.

[11] D. E. Alsdorf, J. M. Melack, T. Dunne, L. A. K. Mertes, L. L. Hess, and L. C. Smith, "Interferometric radar measurements of water level changes on the Amazon flood plain," *Nature*, vol. 404, pp. 174–177, 2000.

[12] E. R. Stofan, D. L. Evans, C. Schmullius, B. Holt, J. J. Plaut, J. van Zyl, S. D. Wall, and J. Way, "Overview of results of spaceborne imaging radar-C, X-band synthetic aperture radar (SIR-C/X-SAR)," *IEEE Trans. Geosci. Remote Sensing*, vol. 33, pp. 817–828, July 1995.

[13] L. L. Hess, Ph.D. dissertation, Univ. California, Santa Barbara, 1999.

[14] H. A. Zebker and J. Villasenor, "Decorrelation in interferometric radar echoes," *IEEE Trans. Geosci. Remote Sensing*, vol. 30, pp. 950–959, July 1992.

[15] F. K. Li and R. M. Goldstein, "Studies of multibaseline spaceborne interferometric synthetic aperture radars," *IEEE Trans. Geosci. Remote Sensing*, vol. 28, pp. 88–97, Jan. 1990.

[16] P. A. Rosen, S. Hensley, H. A. Zebker, F. H. Webb, and E. J. Fielding, "Surface deformation and coherence measurements of Kilauea Volcano, Hawaii, from SIR-C radar interferometry," *J. Geophys. Res.*, vol. 101, pp. 23 109–23125, 1996.

[17] D. Massonnet and T. Rabaute, "Radar interferometry: Limits and potential," *IEEE Trans. Geosci. Remote Sensing*, vol. 31, pp. 455–464, May 1993.

[18] H. A. Zebker, P. A. Rosen, S. Hensley, and P. J. Mouginis-Mark, "Analysis of active lava flows on Kilauea volcano, Hawaii, using SIR-C radar correlation measurements," *Geology*, vol. 24, pp. 495–498, 1996.

[19] E. Rignot, "Dual-frequency interferometric SAR observations of a tropical rain-forest," *Geophys. Res. Lett.*, vol. 23, pp. 993–996, 1996.

[20] L. C. Smith and D. E. Alsdorf, "Control on sediment and organic carbon delivery to the Arctic Ocean revealed with space-borne synthetic aperture radar: Ob' River, Siberia," *Geology*, vol. 26, pp. 395–398, 1998.

[21] U. Wegmuller and C. Werner, "Gamma SAR processor and interferometry software," in *3rd ERS Scientific Symp.*, Florence, Italy, Mar. 17–21, 1997.

[22] Exercito do Brasil Servico Geografico, 1:100 000 Scale Topographic Maps, 1978–1980.

[23] R. M. Goldstein, H. A. Zebker, and C. L. Werner, "Satellite radar interferometry: Two-dimensional phase unwrapping," *Radio Sci.*, vol. 23, pp. 713–720, 1988.

[24] H. A. Zebker, C. L. Werner, P. A. Rosen, and S. Hensley, "Accuracy of topographic maps derived from ERS-1 interferometric radar," *IEEE Trans. Geosci. Remote Sensing*, vol. 32, pp. 823–836, July 1994.

[25] H. A. Zebker, P. A. Rosen, and S. Hensley, "Atmospheric effects in interferometric synthetic aperture radar surface deformation and topographic maps," *J. Geophys. Res.*, vol. 102, pp. 7547–7563, 1997.

[26] R. Goldstein, "Atmospheric limitations to repeat-track radar interferometry," *Geophys. Res. Lett.*, vol. 22, pp. 2517–2520, 1995.

[27] L. F. W. Lesack and J. M. Melack, "Flooding hydrology and mixture dynamics of lake water derived from multiple sources in an Amazon floodplain lake," *Water Resources Res.*, vol. 31, pp. 329–345, 1995.

[28] A. L. Gray and P. J. Farris-Manning, "Repeat-pass interferometry with airborne synthetic aperture radar," *IEEE Trans. Geosci. Remote Sensing*, vol. 31, pp. 180–191, Mar. 1993.

[29] D. R. Stevens, I. G. Cumming, and A. L. Gray, "Options for airborne interferometric SAR motion compensation," *IEEE Trans. Geosci. Remote Sensing*, vol. 33, pp. 409–420, Mar. 1995.

[30] J. M. Melack and B. R. Forsberg, "Biogeochemistry of Amazon floodplain lakes and associated wetlands," in *The Biogeochemistry of the Amazon Basin and its Role in a Changing World*, M. E. McClain, R. L. Victoria, and J. E. Richey, Eds. New York: Oxford Univ. Press.

[31] E. Matthews and I. Fung, "Methane emission from natural wetlands: Global distribution, area, and environmental characteristics of sources," *Global Biogeochemical Cycles*, vol. 1, pp. 61–86, 1987.

[32] E. Matthews, "Wetlands," in *Atmospheric Methane: Sources, Sinks, and Role in Global Change*, M. A. K. Khalil, Ed. Berlin, Germany: Springer-Verlag, 1993, pp. 314–361.

[33] B. Chapman, V. Taylor, and A. Rosenqvist, "Rain forest mapping project to release CD-ROMs," *EOS Trans. Amer. Geophys. Union*, vol. 79, p. 417, 1998.

Douglas E. Alsdorf received the B.A. in geology and the M.Sc. in geophysics from The Ohio State University, Columbus, in 1986 and 1991, respectively, and the Ph.D. in geophysics from Cornell University, Ithaca, in 1996.

Presently, he is an Assistant Research Scientist with the Institute for Computational Earth System Science, University of California, Santa Barbara. His research interests include the use of reflection seismology and potential field data to understand crustal deformation and the study of floodplain hydrology using interferometric synthetic aperture radar.

Laurence C. Smith received the B.S. in geology from the University of Illinois, Urbana, in 1989, the M.S. in geological sciences from Indiana University, Bloomington, in 1991, and the Ph.D. in geological sciences from Cornell University, Ithaca, NY, in 1996.

His research includes remote sensing of river properties, wavelet analysis of streamflow time series, and the use of SAR interferometry in arctic and alpine hydrology. He is currently an Assistant Professor with the Department of Geography, University of California, Los Angeles.

John M. Melack, photograph and biography not available at the time of publication.